CEAS-GNC-2024-069

EuroGNC Navigation Guidance Control CEAS Bristol, UK June 11th-13th 2024
University of BRISTOL ROYAL AERONAUTICAL SOCIETY AIAA

Design and Flight Testing of a Feedback-Linearising Control Law for a Large Flight Envelope on a Sub-Scale Airliner

Daniel Pusztai PhD Student, University of Bristol, School of Civil, Aerospace & Design Engineering, BS8 1TR, Bristol, United Kingdom. daniel.pusztai.2019@bristol.ac.uk

Mark H. Lowenberg Professor of Flight Dynamics, University of Bristol, School of Civil, Aerospace & Design Engineering, BS8 1TR, Bristol, United Kingdom. m.lowenberg@bristol.ac.uk

Simon A. Neild Professor of Nonlinear Structural Dynamics, University of Bristol, School of Civil, Aerospace & Design Engineering, BS8 1TR, Bristol, United Kingdom. simon.neild@bristol.ac.uk

ABSTRACT

A new flight control law for transport aircraft to improve performance beyond the normal flight envelope is presented. It consists of a longitudinal, lateral, and directional control and stability augmentation system and has three main features: 1) Feedback linearisation to cancel the effects of the aircraft's nonlinear aerodynamics; 2) Proportional-integral-derivative control with gain scheduling to improve the overall system dynamics and facilitate command tracking; 3) Command shaping functions with feedforward paths to achieve good handling qualities. Flight envelope protection is achieved by limiting the pilot's control inputs depending on the airspeed and vehicle configuration. The control law was implemented and test-flown on a remotely-piloted 3.7% scale model of NASA's Generic T-Tail Transport aircraft configuration. Flight tests are compared to simulation studies to evaluate the robustness of the developed controllers. The results include lateral-directional control during stalled flight, angle of attack limitation during slow level flight, and a single engine failure scenario with automatic yaw coordination. Some results are also compared to the unaugmented system and a simple linear roll/yaw damper to prove the benefits of a nonlinear control law.

Keywords: flight control law, feedback linearisation, flight envelope protection, transport aircraft, flight testing

Nomenclature

b_W	=	wing span
$\bar{c}_W$	=	wing mean aerodynamic chord
C_{ij}	=	aerodynamic derivative of i with respect to j
C_l, C_m, C_n	=	body-axis moment coefficients
C_L	=	lift coefficient
C_X, C_Y, C_Z	=	body-axis force coefficients
f_S	=	sample rate
$F_{\bullet}$	=	nonlinear gain
g	=	gravitational acceleration
$H_{\bullet}$	=	transfer function
$I_{\bullet}$	=	moment of inertia
$K_{\bullet}$	=	controller gain
n	=	load factor
P, Q, R	=	body-axis roll, pitch, yaw rates
S_W	=	wing area
$T_{\bullet}$	=	controller time constant
u	=	input vector

v	= transformed input vector	δ_E	= elevator deflection
V_I, V_T	= indicated, true airspeed	δ_I	= stabiliser deflection
V_{ref}	= reference airspeed	δ_R	= rudder deflection
V_S	= 1 g stall speed	δ_{roll}	= pilot roll stick input
w	= control error	δ_{pitch}	= pilot pitch stick input
x	= state vector	δ_{yaw}	= pilot yaw stick input
α	= angle of attack	Δcg	= relative centre of gravity location from moment reference
α_0	= trim angle of attack		
β	= sideslip	ρ	= air density
δ_A	= aileron deflection	ϕ, θ, ψ	= Euler bank, pitch, yaw angle

1 Introduction

Stability augmentation systems are an integral part of all modern transport aircraft and range from simple yaw dampers to complex fly-by-wire systems with flight envelope protections. To date, flight control laws are mostly designed according to classical control theory: a linear control scheme is tuned on a linearised flight dynamical model [1]. Gain scheduling is used to account for variations in the operational parameters, such as airspeed and density altitude. This process is adequate, since transport aircraft operate within a narrow flight envelope during normal operations and the control inputs required to maintain a trimmed state are small. But situations can arise that impair the effectiveness of conventional linear flight control laws, such as equipment failures, manoeuvring at the edge of the flight envelope, and departure from controlled flight [2–3]. The latter is also referred to as an upset, during which a very high angle of attack (AoA) and sideslip angle can be encountered. The difficulty of designing a successful feedback system lies in the highly nonlinear aircraft dynamics under upset conditions, such as quickly changing stability derivatives, loss of control authority, and the existence of multiple steady state solutions [4].

The flight control law presented in this paper was developed to improve the handling qualities of a remotely-piloted sub-scale transport aircraft. It employs feedback linearisation to compensate for the most dominant aerodynamic nonlinearities. The control scheme is implemented as a cascaded system with two loops. The inner loop uses a feedback-linearising controller designed to approximate the linear aircraft dynamics at a reference airspeed independent of AoA. Additionally, the effects of changes in the aircraft weight and balance are also compensated here. The outer loop adds a proportional-integral-derivative (PID) controller to improve the overall system dynamics and tracking of command inputs. This flight control law is split into three separate command and stability augmentation systems (CSAS) for the longitudinal, lateral, and directional axes, which can be decoupled and used separately. The command inputs to the three CSAS are AoA, bank angle, and sideslip respectively. Pilot stick commands for elevator, aileron, and rudder are mapped to these inputs through command shaping functions, which allow utilisation of the full flight envelope while ensuring good handling qualities independent of the aircraft state and configuration.

The flight control law was implemented on a remotely-piloted 3.7% scale model of NASA's Generic T-Tail Transport (GTT) aircraft configuration (Fig. 1). The GTT is a hypothetical aircraft and resembles a typical regional jet airliner. It was developed by the NASA Langley Research Center to study upset dynamics of transport aircraft [5–6]. NASA conducted wind tunnel tests, computational fluid dynamic analysis, and simulation studies on the GTT and shared the geometry and aerodynamic data with the University of Bristol (UoB) to conduct further research. Subsequently, three different 3.7% dynamically-scaled models of the GTT were designed and built by the author at the UoB. These models were used in both wind tunnel [7] and free-flight testing [8] and provided an extensive aerodynamic dataset for the flight control law design task.

Fig. 1 University of Bristol's remotely-piloted GTT model in flight

The presented flight control laws were test flown by the author on the UoB's GTT model. Their performance and robustness are assessed through three test cases discussed in this paper:

1. Lateral-directional control during stalls at up to 30° AoA.
2. High-alpha protections during slow flight with all three CSAS active.
3. A single engine failure with automatic compensation of the ensuing asymmetric state.

Some of the flight test data is also compared to simulation results in order to assess the robustness of the control law in the presence of modelling uncertainties of the underlying nonlinear aerodynamic coefficients.

2 Generic T-Tail Transport Model

The GTT is an aircraft model defined by the NASA Langley Research Center to study upset dynamics and control schemes of T-tailed aircraft. It resembles a typical regional jet with a swept-back wing, aft-mounted turbofan engines, and a high stabiliser (T-tail). Apart from its geometric dimensions, the GTT model also defines nominal specifications for mass, moment of inertia, centre of gravity (C.G.), and control surface deflections. The aircraft geometry and aerodynamic data was shared with the UoB in order to conduct further research and a 3.7% scale wind tunnel model and two remotely-piloted models were subsequently built at the UoB (Fig. 2). In a previous wind tunnel campaign at the UoB, static force and moment measurements, as well as tuft pictures were collected over a wide envelope up to 60° AoA and 35° sideslip with several control surface deflections [7]. Additionally, flight tests were carried out with the remotely-piloted vehicles to gather data under normal and upset flight conditions for system identification studies [8].

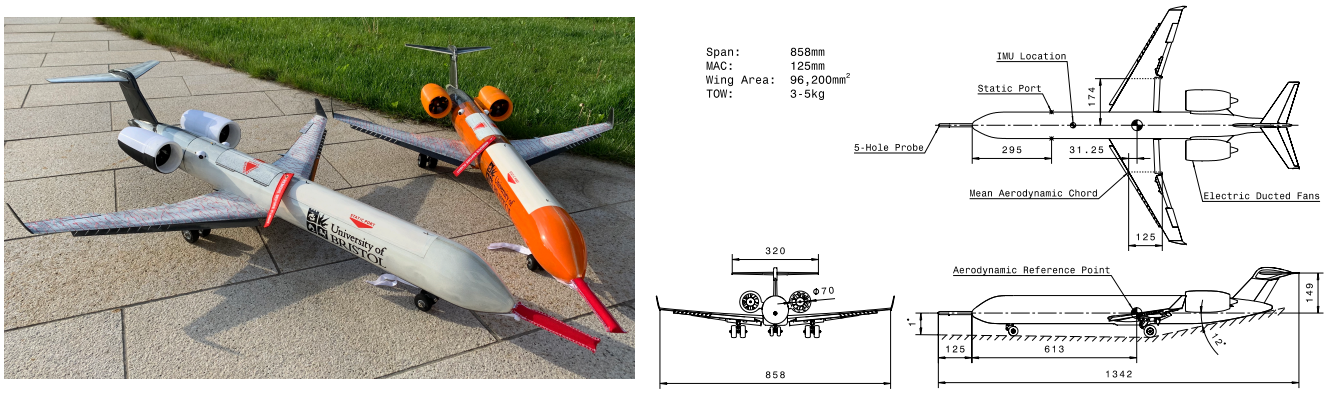

(a) Flight test vehicles (b) Dimensional drawing

Fig. 2 GTT remotely-piloted model

2.1 Aerodynamic Characteristics

The GTT exhibits several aerodynamic nonlinearities, which are mostly driven by its high wing sweep, rear-mounted engine nacelles, small vertical stabiliser, and T-tail empennage. Since these features are commonly found on many modern transport aircraft configurations, similar aerodynamic characteristics can be expected. The aerodynamic coefficients in figures 3a–b have been collected during wind tunnel tests at the UoB and reveal some of these nonlinearities. The data in these plots is shown for the configuration of the remotely-piloted vehicle as pictured in figure 2b, that is with the high-lift devices and landing gear extended. All moment coefficients are referenced to the aerodynamic reference point at 25% of the mean aerodynamic chord (MAC). The relative location of the C.G. is then defined as:

$$\Delta cg = \frac{C.G.[\%] - 25\,\%}{100\,\%} \tag{1}$$

Figure 3a shows the pitching moment coefficient for neutral, full down, and full up elevator deflection. Starting at 8° AoA, the negative pitch curve slope starts to diminish and eventually develops into an unstable pitch break at approximately 12° AoA. This relates to the onset of flow separation at the wing tips (Fig. 4), causing a forward shift of the centre of pressure and a nose up pitch tendency. Beyond 20° AoA, elevator effectiveness decreases as the tail is successively blanketed by the wing and engine nacelles. A similar effect can be seen for the rudder yaw effectiveness $C_{n\delta_R}$ in figure 3b, with a rapid reduction to almost zero yaw authority between 20° and 30° AoA. Figure 3b also shows the aileron roll effectiveness $C_{l\delta_A}$ in dependence of AoA. In this case, the progressing wing tip stall causes a loss of half of the normal aileron control power well before the actual stall AoA of 12° is reached. This effect is also responsible for a degradation of roll damping during an approach to stall, causing a violent wing rock. Some of these phenomena are dependent on Reynolds number and while the data in this paper relates to the sub-scale model tests, it is anticipated that the full-scale aircraft will exhibit qualitatively similar characteristics [6].

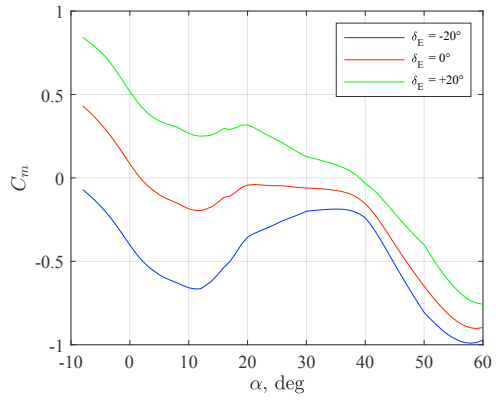

(a) Pitching moment for several elevator deflections

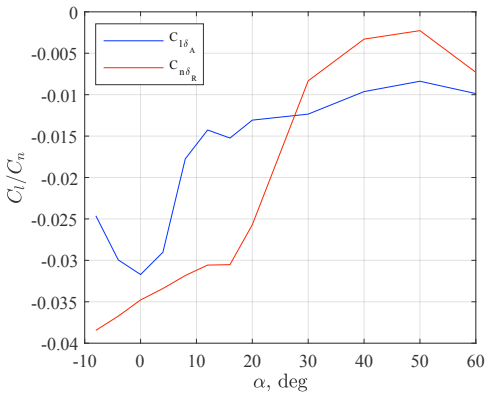

(b) Aileron-roll and rudder-yaw control authority

Fig. 3 GTT aerodynamic characteristics in dependence of AoA (high lift configuration)

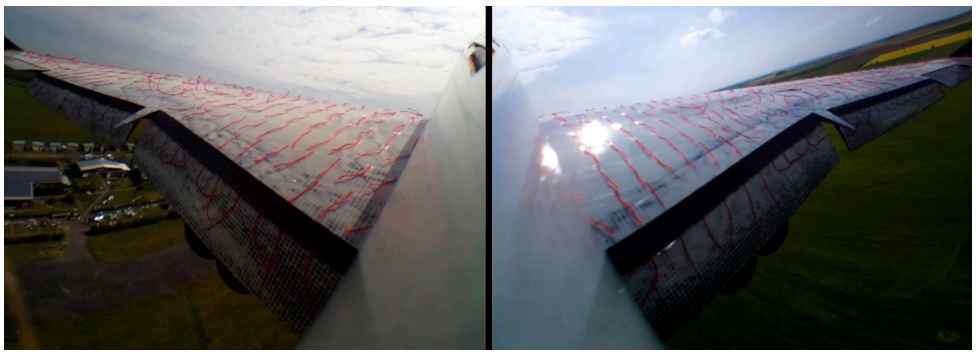

Fig. 4 Tuft picture of wing tip stall during GTT flight test

2.2 Remotely-Piloted Vehicle

The flight control laws presented in this paper were tested on the GTT remotely-piloted vehicles (Fig. 2). Each plane is equipped with a custom built flight control and instrumentation system, which is schematically depicted in figure 5. All on-board sensors, actuators, and radio links are controlled by a 32-bit flight computer clocked at 170 MHz. It executes purpose-made software written in *C++* that also handles the inertial navigation system (INS), the air data system (ADS), flight control law computations, data up- and downlink, and data logging in a 50 Hz main loop. This centralised approach minimises the computational delays in the system, which is critical for the high bandwidth of dynamically scaled aircraft. Exact processing times depend on several factors, but are at most 34 ms from sensor inputs to control outputs.

The full vehicle state vector is obtained by combining multiple sensor sources, which are sampled synchronously at rates between 50 and 800 Hz. The obtained data is filtered by digital Butterworth and Bessel lowpass filters, with cut-off frequencies and filter orders selected to balance signal smoothness against group delay. Acceleration, angular rate, and magnetic field data from the inertial measurement unit (IMU) is used by the INS together with position data from the global navigation satellite system (GNSS) receiver to estimate the inertial states through a Kalman filter. The ADS calculates the vehicle's relative air speed and density altitude from five pressure sources: two static pressure sensors on each fuselage side and three differential pressure sensors connected to a 5-hole probe nose boom. The pneumatic system was calibrated in the wind tunnel and is capable of measuring AoA and sideslip up to 45° with an absolute accuracy between ±1° (low incidence) and ±3° (high incidence).

The control surfaces are actuated by commercial off-the-shelf (COTS) high-speed servo motors. Their response times were fast enough to be neglected during the tuning of the control laws, but the final designs were validated through simulations that included nonlinear servo models. Actuator dynamics were identified from bench tests, which showed bandwidths of 3–9 Hz, depending on the deflection amplitude. Propulsion is provided by two electric ducted fan engines. Each aircraft is also equipped with a ballistic parachute recovery system, that allows safe termination of stall tests down to very low altitudes. The pilot controls the model through a COTS handheld radio transmitter with the ability to switch the active flight control laws at any time during flight. Data is sent to a ground station which allows monitoring of the system status and test execution. Additionally, up to 128 floating point parameters are logged on-board at 50 Hz for post-flight evaluation. A custom hardware-in-the-loop (HIL) simulation environment was created to assist with pilot training, control law evaluation, test planning, and software checkouts. It consists of a 3D visualisation with a realtime six-degrees-of-freedom (6-DOF) *Simulink* model, simulating the aircraft aerodynamics, equations of motion, flight controls, propulsion system, sensor characteristics, landing gear dynamics, and wind effects.

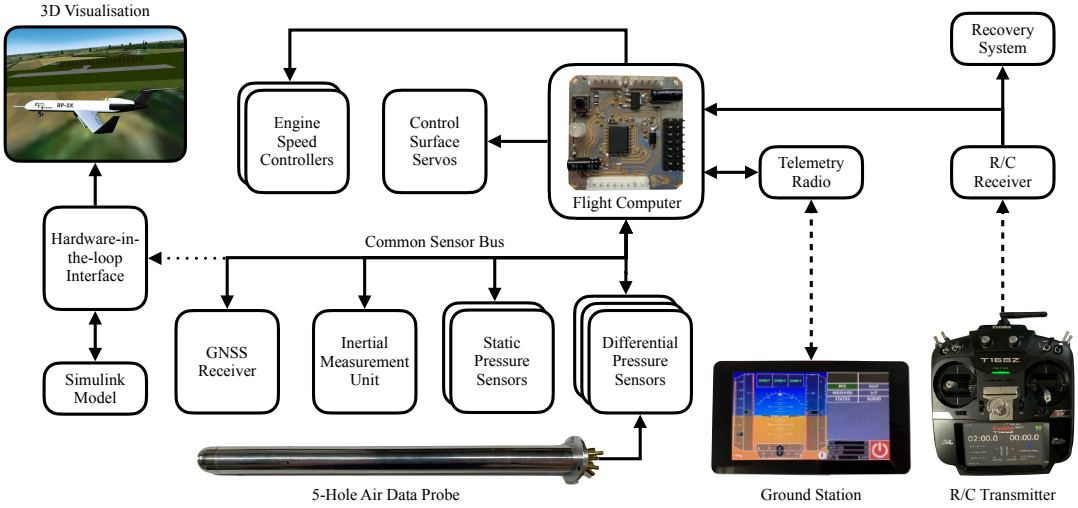

Fig. 5 Flight control and instrumentation schematic

3 Flight Control Laws

Figure 6 shows a schematic diagram of the presented flight control law, which has been designed to address the key stability issues described in section 2.1. This is achieved by compensating the most dominant aerodynamic nonlinearities in the inner feedback linearisation loop of the control law. For this, the aircraft dynamics are written as an input affine system of the form:

$$\dot{x} = f(x) + g(x)\,u \tag{2}$$

Here $f(x)$ and $g(x)$ are nonlinear functions that have to be compensated. Now the nonlinear control law

$$u = -\,r(x) + q(x)\,v \tag{3}$$

with the feedback function $r(x)$ and a pre-filter $q(x)$ transforms the inner loop dynamics into a linear system. Generally, these functions consist of aerodynamic derivatives, which are nonlinear in AoA. The feedback-linearising controller is designed to approximate the linearised dynamics of the aircraft at the reference flight speed $V_{ref} = 1.3\,V_S$. This allows the use of a conventional PID controller in the outer loop to improve the system dynamics and tracking of command values:

$$v(t) = K_P \left(w(t) + \frac{1}{T_I} \int_0^t w(\tau)\,d\tau \right) + K_D \frac{dw(t)}{dt} \tag{4}$$

The three controller parameters are the proportional gain K_P, derivative gain K_D, and integrator time constant T_I. The latter is selected to be equal to the short-period and Dutch-roll natural frequencies for the longitudinal and lateral-directional axes respectively. The proportional and derivative gains are tuned to achieve a desired crossover frequency (selected based on realisable system dynamics) and a minimum phase margin of 45° through common techniques for linear time-invariant systems. If constant gains were to be used in the outer loop PID controller, the aircraft would show a similar control response at any flight condition due to the feedback-linearising inner loop. This is not desirable since the full aircraft performance can not be utilised (i.e. a controller tuned for high flight speeds will not utilise all of the available control authority at slow speed) and the aircraft's behaviour at different flight speeds will feel unnatural to the pilot. The PID controller parameters are therefore gain-scheduled to mimic the natural aircraft dynamics with varying indicated airspeed:

$$K_P = K_{P0} \left(\frac{V_I}{V_{ref}} \right)^2 \qquad K_D = K_{D0}\,\frac{V_I}{V_{ref}} \qquad T_I = T_{I0}\,\frac{V_{ref}}{V_I} \tag{5}$$

Command inputs to the controller are generated from pilot stick inputs through a command shaping function that adjusts the available flight envelope depending on the current aircraft state. To improve the tracking response of the controller, a feedforward path additionally generates trimmed control surface deflections directly from the command inputs. The control law is separately implemented for the longitudinal, lateral, and directional axes. These three CSAS have been designed together, but can function independently from each other if required.

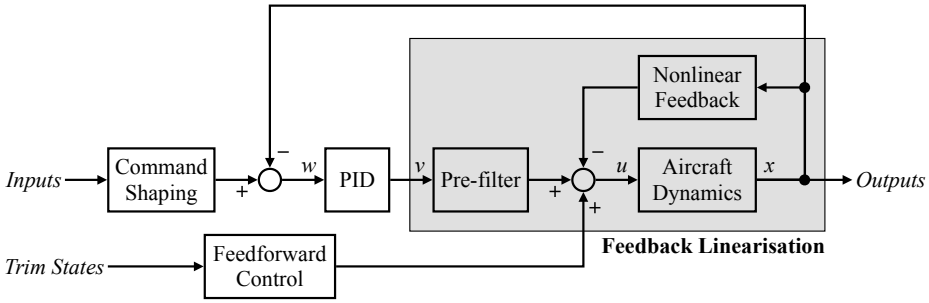

Fig. 6 Schematic flight control law

3.1 Longitudinal CSAS

The longitudinal CSAS is shown in figure 7. All nonlinear functions in the schematic are summarised in the appendix. For the inner loop controller design, the rotational rigid-body equation of motion for the pitch axis is written as:

$$\dot{Q} = q_\infty \frac{S_W \bar{c}_W}{I_{yy}} \Big[C_{m0}(\alpha) - \Delta cg\, C_{Z0}(\alpha) + \left(C_{m\hat{q}}(\alpha) - \Delta cg\, C_{Z\hat{q}}(\alpha) \right) \frac{\bar{c}_W}{2\, V_T} Q + \left(C_{m\delta_E}(\alpha) - \Delta cg\, C_{Z\delta_E}(\alpha) \right) \delta_E + \left(C_{m\delta_I}(\alpha) - \Delta cg\, C_{Z\delta_I}(\alpha) \right) \delta_I \Big] \tag{6}$$

This assumes steady level flight and neglects smaller aerodynamic terms, as well as the pitching moment from engine thrust. Feedback linearisation of above equation is achieved through two nonlinear feedback gains F_α and F_Q and two nonlinear pre-filters F_{qy} and F_{δ_E} according to figure 7. Additionally, the stabiliser is always trimmed through the feedforward function $\delta_I(\alpha_0)$ such that the aircraft maintains the computed trim AoA α_0 with neutral elevator deflection. Below the reference speed V_{ref}, the trim AoA is frozen and a constant pull input is required by the pilot to maintain level flight. This creates an artificial feel for the pilot and indicates that the aircraft is approaching the stall speed. The stabiliser trim law is:

$$\delta_I = - \frac{C_{m0}(\alpha_0) - \Delta cg\, C_{Z0}(\alpha_0)}{C_{m\delta_I}(\alpha_0) - \Delta cg\, C_{Z\delta_I}(\alpha_0)} \tag{7}$$

The theoretical inner loop dynamics with the auto-trim function then become:

$$\dot{Q} = q_\infty \frac{S_W \bar{c}_W}{I_{yy}} \left[C_{maref}(\alpha - \alpha_0) + C_{m\hat{q}ref} \frac{\bar{c}_W}{2\, V_T} Q \right] \tag{8}$$

The inputs to the outer loop PID controller are a target AoA α_{cmd} and pitch rate Q_{cmd}. The former is computed from the pilot input and the current trim AoA through the command shaping function $\alpha_c(\delta)$, which maps the pilot stick inputs either between the minimum and maximum load factor $n_{min/max}$ or the AoA limits $\alpha_{min/max}$, whichever is the limiting. When the lateral CSAS is active, a pitch rate target is computed from the commanded bank angle ϕ_{cmd} according to a steady-state coordinated turn condition. The full elevator control law for both feedback loops finally is:

$$\delta_E = F_{\delta_E} \Big[F_{qy} \Big(K_Q \left(Q_{cmd} - Q \right) + H_\alpha K_\alpha \left(\alpha_{cmd} - \alpha \right) \Big) - F_Q Q - F_\alpha(\alpha, \alpha_0) \Big] \tag{9}$$

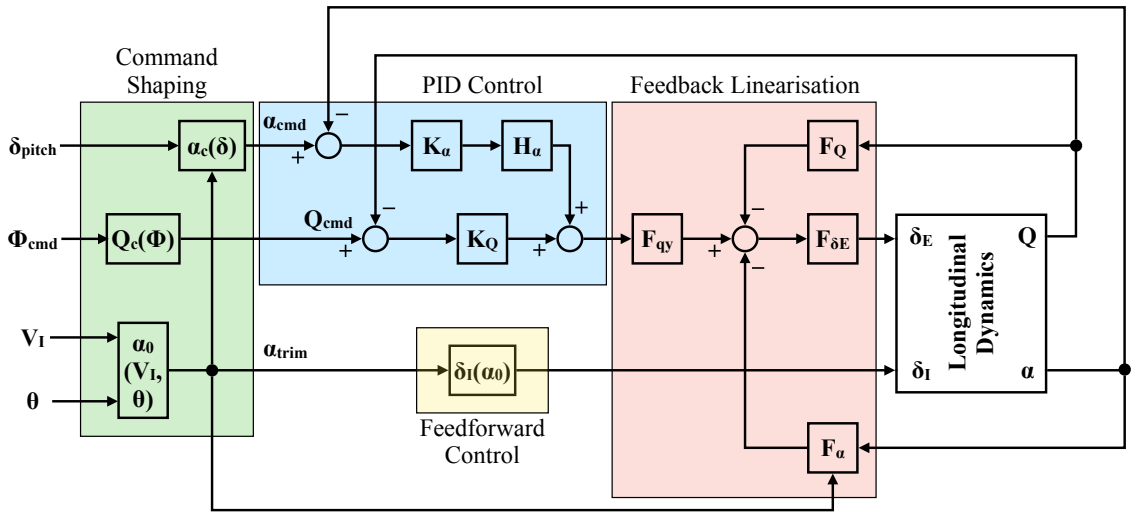

Fig. 7 Longitudinal CSAS schematic

3.2 Lateral-Directional CSAS

For the lateral and directional CSAS design (Fig. 8), the rotational equations of motion are formulated in a similar way as equation 6 by assuming a steady-state flight condition and neglecting small aerodynamic terms:

$$\dot{P} = q_\infty \frac{S_W\, b_W}{I_{xx}} \Big[\Big(C_{l\beta} + \frac{I_{xz}}{I_{zz}} C_{n\beta} \Big) \beta + C_{l\hat{P}} \frac{b_W}{2\, V_T} P + C_{l\delta_A}\, \delta_A + \Big(C_{l\hat{R}} + \frac{I_{xz}}{I_{zz}} C_{n\hat{R}} \Big) \frac{b_W}{2\, V_T} R + \Big(C_{l\delta_R} + \frac{I_{xz}}{I_{zz}} C_{n\delta_R} \Big) \delta_R \Big] \tag{10}$$

$$\dot{R} = q_\infty \frac{S_W\, b_W}{I_{zz}} \Big[\Big(C_{n\beta} + \frac{I_{xz}}{I_{xx}} C_{l\beta} \Big) \beta + \frac{I_{xz}}{I_{xx}} C_{l\hat{P}} \frac{b_W}{2\, V_T} P + \frac{I_{xz}}{I_{xx}} C_{l\delta_A}\, \delta_A + \Big(C_{n\hat{R}} + \frac{I_{xz}}{I_{xx}} C_{l\hat{R}} \Big) \frac{b_W}{2\, V_T} R + \Big(C_{n\delta_R} + \frac{I_{xz}}{I_{xx}} C_{l\delta_R} \Big) \delta_R \Big] \tag{11}$$

Partial feedback linearisation of the lateral-directional dynamics is achieved through feedback of the roll and yaw rate via the nonlinear gains F_P and F_R, as well as the pre-filters F_{qx}, F_{qz}, F_{δ_A}, and F_{δ_R} according to figure 8. Bank angle feedback is not necessary due to the almost neutral spiral stability of the GTT. The static directional stability derivative $C_{n\beta}$ on the other hand varies significantly with AoA, even becoming unstable above 15° AoA. This nonlinearity is not compensated due to insufficient rudder control power at high AoA, which would result in control saturation. Nevertheless, some departure resistance is still provided through a positive dynamic lateral-directional stability coefficient $C_{n\beta}{}^*$ due to the stabilising dihedral effect $C_{l\beta}$ of the GTT [9].

Equations 10–11 are coupled through the angular rates P, R and the control inputs δ_A, δ_R. The cross-control terms $C_{l\delta_R} + I_{xz}/I_{zz}\, C_{n\delta_R}$ and $I_{xz}/I_{xx}\, C_{l\delta_A}$ are not compensated since they actually improve turn coordination and counteract coupling effects during sideslips. Similarly, the cross derivative $C_{l\hat{R}} + I_{xz}/I_{zz}\, C_{n\hat{R}}$ has a stabilising effect on the Dutch-roll mode and is also not compensated. Linearisation of the term $I_{xz}/I_{xx}\, C_{l\hat{P}}$ would in theory be beneficial, but it is not attempted for the GTT due to the limited yaw control authority.

Each CSAS also features an outer loop PID controller. The lateral axis holds a fixed bank angle command until the pilot provides a stick input, which is translated into a roll rate command. The command scheduling functions $P_c(\delta)$ and $\phi_c(P)$ handle the switch between bank angle and roll rate mode and adapt the maximum allowable roll rate throughout the full airspeed range while maintaining a constant control sensitivity for fine stick inputs. In the directional axis, yaw inputs are replaced by a sideslip command, which is limited to a maximum safe value in dependence of airspeed and the allowable sideslip envelope limit β_{max} through the scheduling function $\beta_c(\delta)$. In order to avoid slipping of the aircraft during a turn, a yaw rate command is calculated from the bank angle command through the function $R_c(\phi)$ and used as a target for the directional PID controller. The feedforward control path additionally generates aileron and rudder trim values for steady roll and steady heading sideslip commands, thus improving controller performance for these highly coupled flight conditions. The complete aileron and rudder control laws are:

$$\delta_A = F_{\delta_A} \Big[F_{qx} \Big(K_P \left(P_{cmd} - P \right) + H_\phi\, K_\phi \left(\phi_{cmd} - \phi \right) \Big) - F_{AR_{11}} F_{P\beta}\, \beta_{cmd} - F_{AR_{12}} F_{RP}\, P_{cmd} - F_P\, P \Big] \tag{12}$$

$$\delta_R = F_{\delta_R} \Big[F_{qz} \Big(K_R \left(R_{cmd} - R \right) + H_\beta\, K_\beta \left(\beta_{cmd} - \beta \right) \Big) - F_{AR_{21}} F_{P\beta}\, \beta_{cmd} - F_{AR_{22}} F_{RP}\, P_{cmd} - F_R\, R \Big] \tag{13}$$

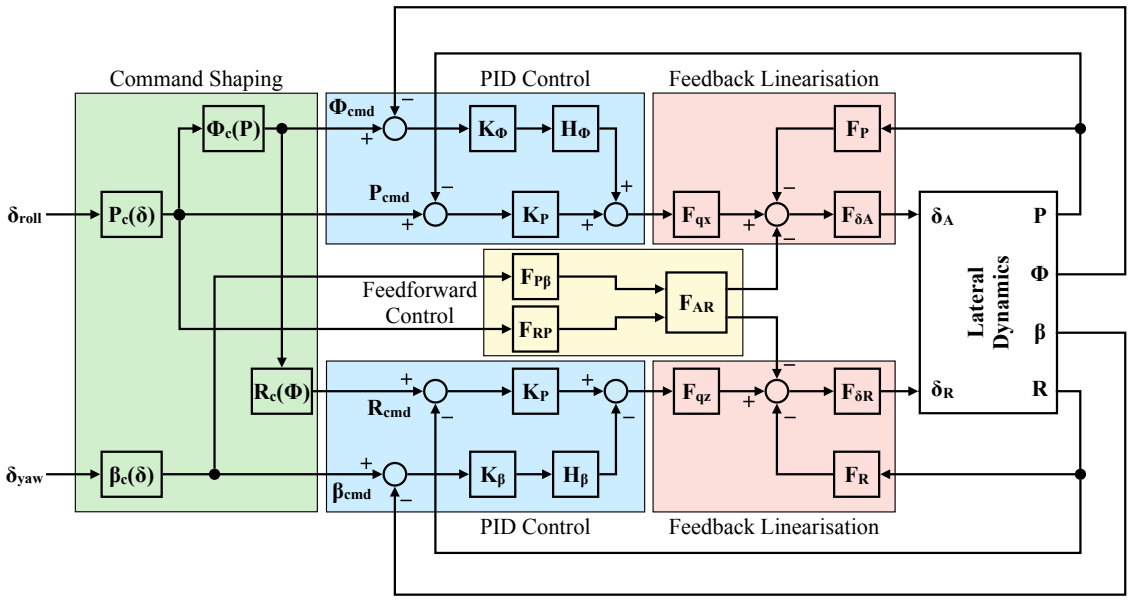

Fig. 8 Lateral CSAS schematic

3.3 Implementation

The control laws were developed and tested in *MATLAB/Simulink*, but for the flight test campaign they had to be implemented in *C++* to run on the on-board flight computer. Calculation of the nonlinear gains for the feedback linearisation and feedforward control requires knowledge of the aerodynamic derivatives in dependence of AoA. These were available only in tabulated form from the wind tunnel test campaign. In order to ensure smoothness and reduce the memory requirements for storing the data, polynomials with up to 7th degree were fitted to the aerodynamic derivatives. It is important to carefully check the fit quality of these polynomials and guard input values from exceeding their valid bounds. The PID control laws were discretised with the Tustin method, which leads to the general form:

$$H_{\bullet} = \frac{s + \frac{1}{T_{\bullet}}}{s} \hat{=} \frac{\left(\frac{1}{2 f_S T_{\bullet}} + 1\right) + \left(\frac{1}{2 f_S T_{\bullet}} - 1\right) z^{-1}}{1 - z^{-1}} \tag{14}$$

Integrator anti-windup protection is achieved by limiting the internal states of this transfer function to the required bounds.

The remotely-piloted vehicles used in the presented test campaign did not have a functional elevator and pitch control was solely achieved through the moveable tailplane. The controller algorithms were left unchanged, but computed elevator commands were added to the stabiliser through a constant relation accounting for the different control effectiveness:

$$\delta_I = \delta_I(\alpha_0) + \frac{C_{m\delta_I}(\alpha_0)}{C_{m\delta_E}(\alpha_0)} \delta_E \tag{15}$$

In practice, the differences in control authority between elevator and stabiliser are small throughout the whole envelope and the simplified mapping from elevator to stabiliser commands is regarded as sufficient.

4 Flight Test Results

This chapter presents several flight test and simulation results to evaluate the effectiveness and robustness of the developed flight control laws.

4.1 Lateral-Directional Control During Stall

One of the design objectives for the lateral-directional CSAS was to be able to stabilise bank and sideslip of the aircraft during all phases of a stall to enable parameter identification tasks of the longitudinal dynamics. Without any feedback augmentation, the vehicle experiences strongly coupled motion in roll, pitch, and yaw during a stall. The aerodynamic effects behind this behaviour were identified through wind tunnel testing and some have been described in section 2.1. Figures 9–10 show accelerated and 1-g stall tests for three different lateral-directional flight control law configurations: direct stick to surface, constant gain roll/yaw damper, and the presented nonlinear CSAS.

The performance benefits of the nonlinear controller can be clearly seen in the accelerated stall tests in figure 9. The CSAS is able to tightly control both bank and sideslip angles even at high AoA due its adjustment of the control surface gains. This effect of the inner loop feedback-linearisation is also easily visible in the increased aileron and rudder outputs at high AoA. Good control of the sideslip angle also avoids the excessive yaw divergence as experienced with the other two cases. Compared to the unaugmented case, the linear rate damper is also able to slightly reduce the bank and sideslip angle excursions at high AoA. But since this controller has been tuned for good performance at the reference airspeed only, it is unable to fully cope with the loss of control effectiveness during post-stall flight.

Figure 10 shows three 1-g stall tests that were conducted by a gradual airspeed reduction in level flight. The unaugmented case reveals the extreme wing rock motion that starts well before the critical AoA is reached due to early wing tip flow separation (Fig. 4) and kinematically couples AoA with sideslip oscillations. Both the linear and nonlinear controllers are able to suppress these oscillations and yield a more defined pitch departure at stall, but bank and yaw excursions are slightly higher for the former. A stable deep-stall is reached in all three cases after five seconds. In this condition, the high control gains of the CSAS eventually cause saturation of the ailerons and rudder.

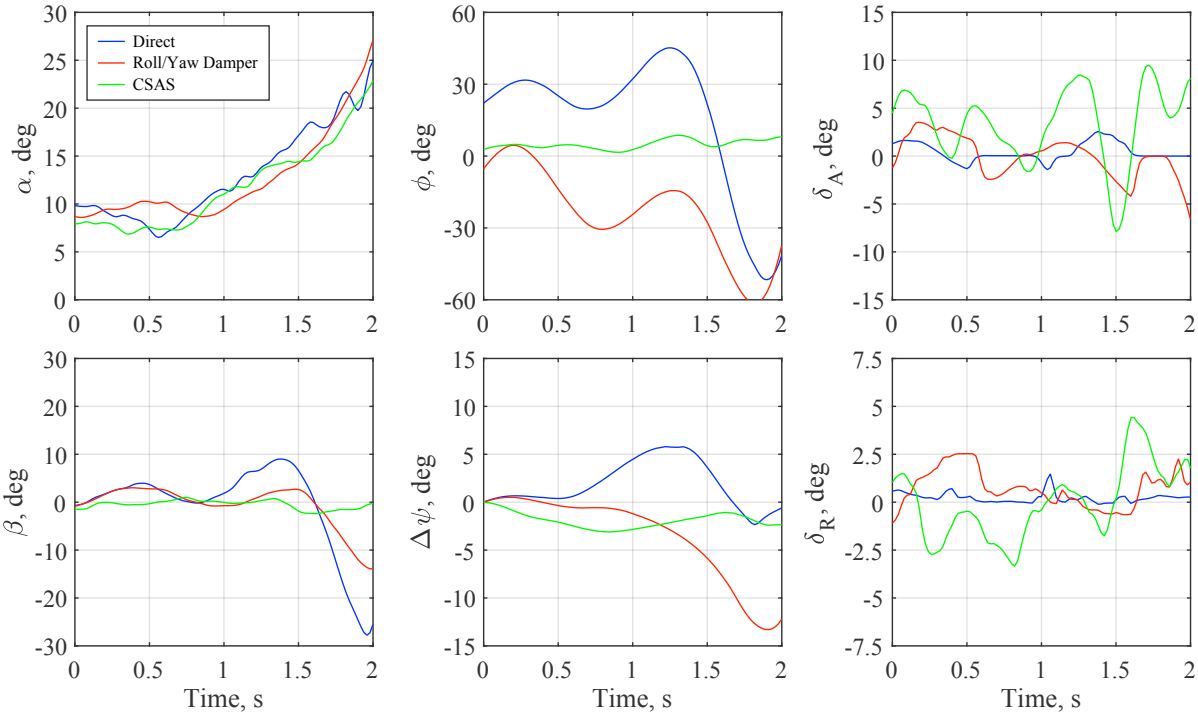

Fig. 9 Lateral-directional dynamics during accelerated stalls with different flight control laws

Figure 11 shows the tracking performance of the CSAS during bank manoeuvres at slow flight speeds and high AoA, ending with an intentional full stall at the nine second mark. All four commanded parameters (bank angle, sideslip, roll rate, and yaw rate) are tracked very well and the adaption of the control surface gains as the AoA changes is apparent. The yaw rate command is generated by the feedforward path from the bank angle command, successively improving turn coordination and ensuring symmetric flight conditions. Also shown in figure 11 is a simulation result based on the initial conditions at the beginning of the test window and the recorded CSAS commands. It was obtained with a 6-DOF flight mechanical model, which includes the aerodynamic database from wind tunnel results and an emulation of the same control laws that are executed on the flight computer.

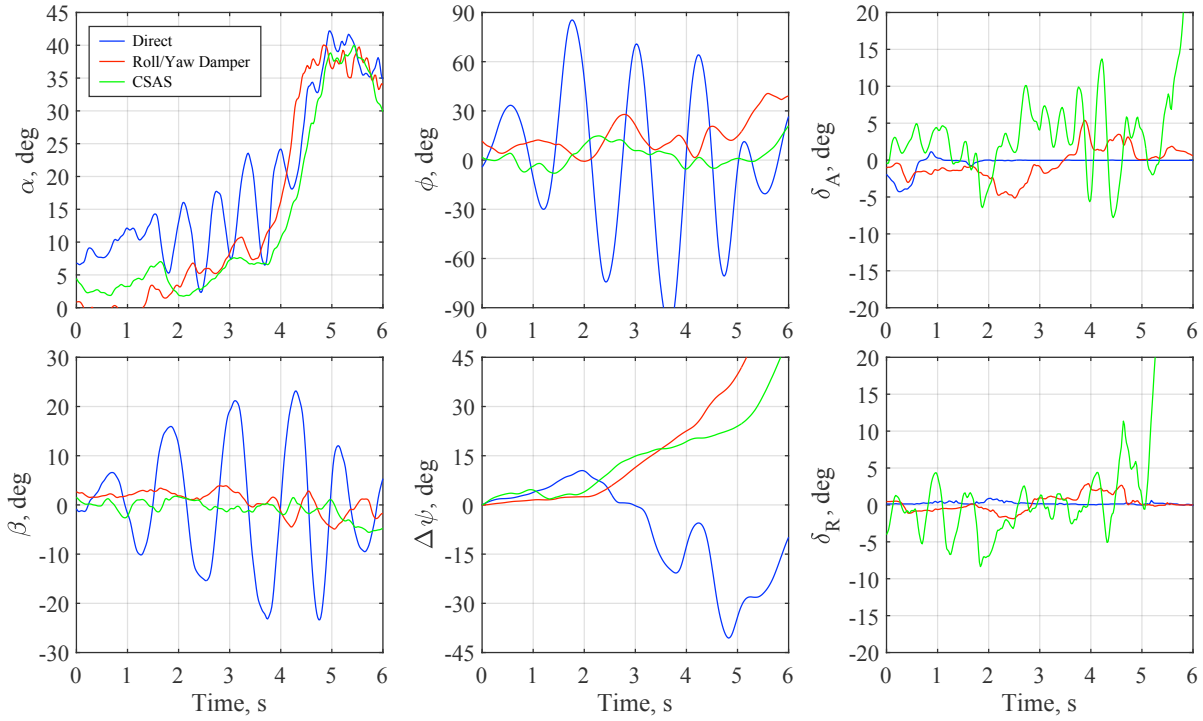

Fig. 10 Lateral-directional dynamics during 1-g stalls with different flight control laws

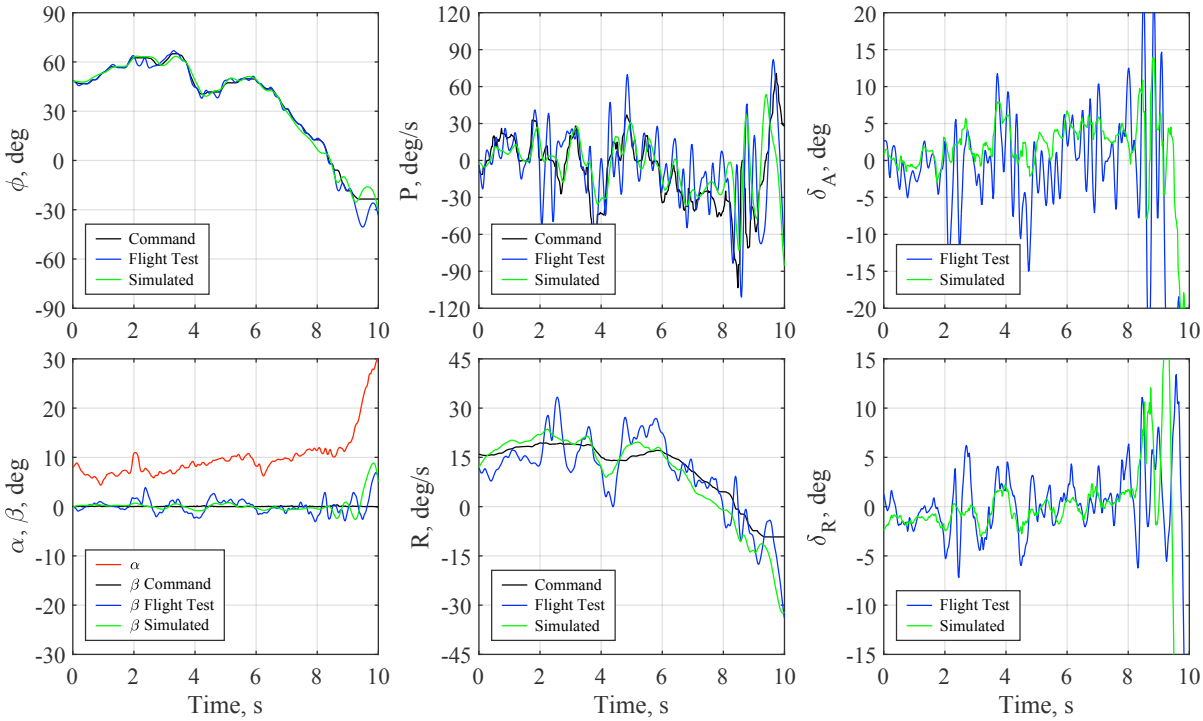

Fig. 11 Lateral CSAS tracking performance during roll manoeuvres at high AoA

The nonlinear feedback gains of the lateral controller were designed with wind tunnel data. Some derivatives were not available for the high-lift wing configuration of the remotely-piloted models and therefore had to be taken from the clean wing data. It was later established through parameter identification from flight test data, that this assumption indeed introduced a discrepancy from the actual derivatives [8]. Nevertheless, no significant performance deficits were observed for the CSAS implementation that was used throughout the test campaign. This suggests that the feedback-linearisation of aileron effectiveness and roll damping is sufficiently robust against small uncertainties, which is also evident from the good agreement between flight test and simulation results in figure 11.

4.2 Longitudinal Control During High-Alpha Flight

The design aim of the longitudinal CSAS was to reduce pilot workload by protecting the aircraft from exceeding the stall AoA during typical flight manoeuvres. For unaugmented flight, a high safety margin to the unstable pitch break shortly before stall, which can cause rapid uncommanded pitch-ups, is required. The CSAS allows safe flight closer to the stall AoA, which in turn reduces the minimum operational flight speed of the aircraft. The envelope protection functionality is implicitly given by the design of the AoA law and the command shaping functions.

Figure 12 shows the results of a flight test during which the speed was successively reduced by increasing the controller's AoA command in level flight. The AoA was limited to 10° after ten seconds with a full back stick input from the pilot. Although the aircraft remained in control throughout the test, high AoA and pitch oscillations were experienced below the reference speed. These oscillations were induced by the controller and ceased as soon as the recovery was initiated around the 14 seconds mark.

Parameter identification tasks from other flight tests suggested a modelling inaccuracy in the static pitch moment curve near stall [8]. Based on these observations, the wind tunnel pitch curve was adjusted as shown in figure 13a. The modifications include a shift of the unstable pitch break towards lower AoA, a change in the pitch coefficient slope and magnitude near stall, and a hysteresis effect when going through the stall region. A simulation of the closed-loop system with both the reference and modified pitching moment curve was conducted with the same initial conditions and command inputs as the flight test shown in figure 12. To assess the controller tracking performance with external disturbances, a small amount of Gaussian noise was added to the simulation states to mimic sensor noise. While the simulation with the original wind tunnel data shows good performance of the control law, its response is severely degraded with the modified pitch moment curve. Similarly to the flight test results, AoA oscillations grow as the command target approaches the limit of 10°.

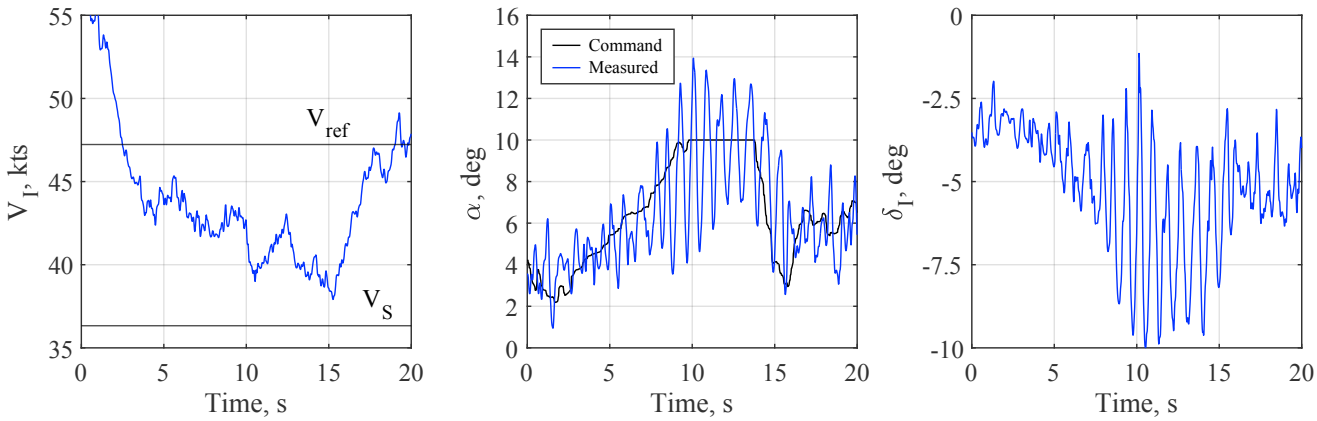

Fig. 12 Longitudinal CSAS tracking performance during slow flight with AoA limiting

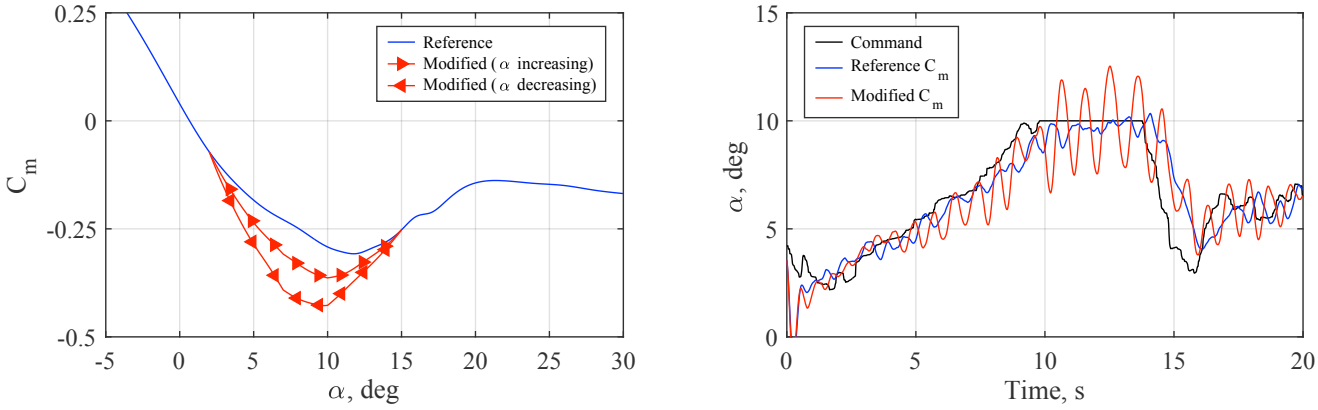

(a) Modified static pitch moment curve

(b) Simulated controller response

Fig. 13 Longitudinal CSAS robustness to modelling inaccuracies

4.3 Single Engine Failure

Due to the dangerous nature of upset testing and the high operational complexity of the aircraft models, a few unscheduled incidents were encountered over the course of the flight test campaign. In all cases, the flight control laws were at least partially active and prevented an otherwise unavoidable loss of control. One such example is the engine failure shown in figure 14. Two seconds into the shown timeframe, the right hand engine shuts down and the model flies with a large thrust asymmetry for approximately four more seconds. This condition was successfully countered by the flight controller with very large rudder and aileron deflections, while the airspeed continuously dropped well below the normally safe reference speed. Excellent manoeuvrability was maintained throughout this incident and the large bank angle commands were precisely tracked. Eventually, the vehicle was safely recovered through deployment of the parachute. This example showcases the capabilities of the presented flight control laws under abnormal flight conditions.

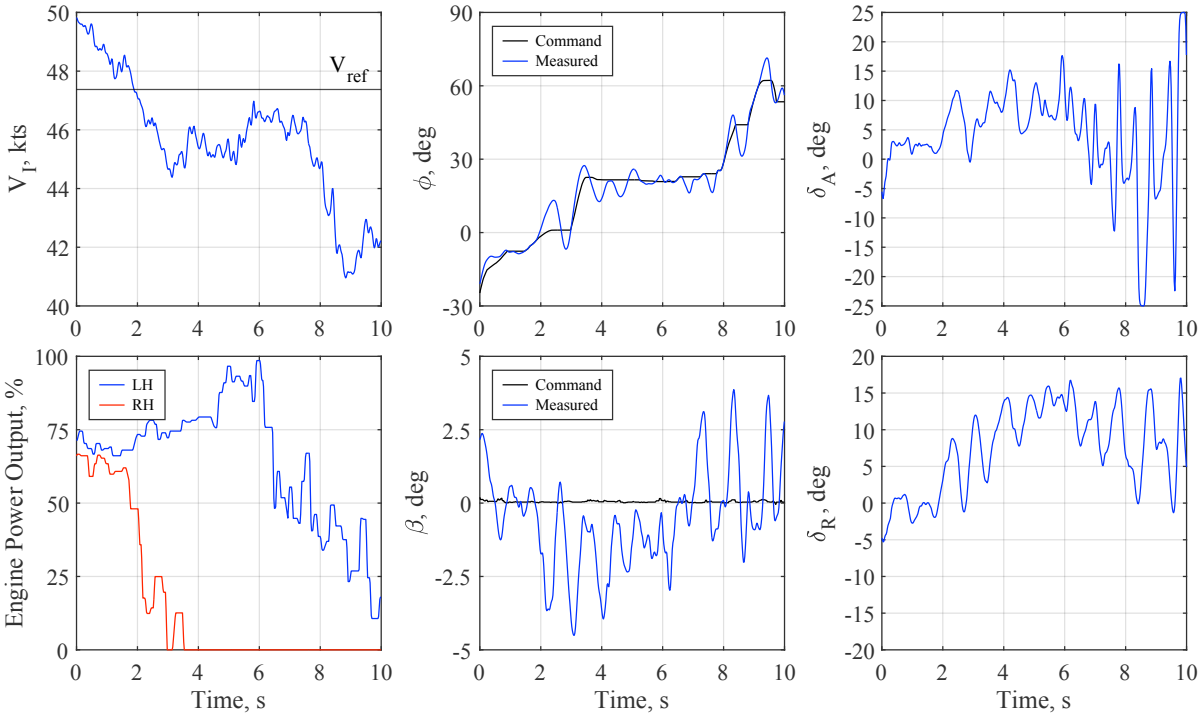

Fig. 14 CSAS performance during asymmetric engine failure

5 Conclusion

The presented longitudinal and lateral-directional flight control laws were developed in support of a flight test campaign conducted on remotely-piloted models of the NASA GTT aircraft. Nonlinear aerodynamics were identified to be linked to undesirable flight characteristics such as wing rock and sudden pitch departure near stall. The handling characteristics of the aircraft were successfully improved by implementing a feedback-linearising control law, which was validated through flight tests. The lateral-directional CSAS showed excellent performance across a wide AoA range during controlled stall tests. The benefit of a nonlinear feedback controller was proven by directly comparing it to test results of a simple linear roll/yaw damper. The lateral CSAS performance was robust in the presence of inaccuracies within the aerodynamic derivatives and matched simulation predictions well. The longitudinal CSAS was more sensitive to modelling uncertainties regarding the pitching moment characteristics near stall and possible error sources were identified and demonstrated through simulations. An improved pitch control law should include these revisions to the aerodynamic model, especially the effects of pitching moment hysteresis near stall.

The experimental test campaign on the UoB GTT aircraft models represents the first time that feedback control laws for a civil transport type were systematically assessed under stalled flight conditions. Compared to the decade-old control algorithms in current state-of-the-art fly-by-wire transport aircraft, which have proven insufficient during upset-related accidents multiple times, the presented nonlinear control laws are an improvement to maintaining control in this critical flight regime where computer stabilisation is desperately required. Even within the normal flight envelope, the developed control laws have proven beneficial with respect to established linear control schemes. For a full-scale application, it is expected that phase margins and relative bandwidths will improve since filter lag, actuator responses, and computational delays are far more limiting in a dynamically scaled model. Naturally, stability and robustness will have to be proven more thoroughly within the normal flight envelope, but flight testing far beyond stall will likely remain practically impossible for full-size transport aircraft in the future, calling for alternative methods like the work presented herein.

Appendix

Parameters of the longitudinal (Fig. 7) and lateral-directional (Fig. 8) CSAS:

Longitudinal CSAS feedback linearisation:

$$F_\alpha = \left(C_{m0}(\alpha) - C_{m0}(\alpha_0)\right) - \Delta cg\left(C_{Z0}(\alpha) - C_{Z0}(\alpha_0)\right) - C_{maref}\left(\alpha - \alpha_0\right)$$

$$F_Q = \frac{\bar{c}_W}{2V_T}\left(C_{m\hat{Q}}(\alpha) - \Delta cg\, C_{Z\hat{Q}}(\alpha) - C_{m\hat{Q}ref}\right)$$

$$F_{\delta_E} = \frac{1}{C_{m\delta_E}(\alpha) - \Delta cg\, C_{Z\delta_E}(\alpha)}$$

$$F_{qy} = \frac{I_{yy}}{q_\infty S_W \bar{c}_W}$$

Longitudinal CSAS command shaping:

$$Q_{cmd} = \frac{g}{V_T}\cdot\frac{\sin^2(\phi_{cmd})}{\cos(\phi_{cmd})}$$

$$\alpha_{cmd} = \begin{cases} \alpha_0 - \delta_{pitch}\left(\alpha_+ - \alpha_0\right) & \ldots \delta_{pitch} \le 0 \\ \alpha_0 + \delta_{pitch}\left(\alpha_- - \alpha_0\right) & \ldots \delta_{pitch} > 0 \end{cases}$$

$$\alpha_0 = \left(\cos(2\theta)\frac{n_0\, m\, g}{q_\infty S_W} - C_{L0}\right)\frac{1}{C_{L\alpha}}$$

$$\alpha_+ = \left(\frac{n_{max}\, m\, g}{q_\infty S_W} - C_{L0}\right)\frac{1}{C_{L\alpha}} \le \alpha_{max}$$

$$\alpha_- = \left(\frac{n_{min}\, m\, g}{q_\infty S_W} - C_{L0}\right)\frac{1}{C_{L\alpha}} \ge \alpha_{min}$$

Lateral CSAS feedback linearisation:

$$F_P = \frac{b_W}{2\,V_T}\left(C_{l\hat{P}}(\alpha) - C_{l\hat{P}ref}\right)$$

$$F_{\delta_A} = \frac{1}{C_{l\delta_A}(\alpha)}$$

$$F_{qx} = \frac{I_{xx}}{q_\infty S_W\, b_W}$$

Lateral CSAS command shaping:

$$P_{cmd} = -P_{ref}\left[1 + \left(\frac{V_I}{V_{ref}} - 1\right)\ \delta_{roll}\ \right]\delta_{roll}$$

$$\phi_{cmd}{}^{(n)} = \phi_{cmd}{}^{(n-1)} + \Delta\phi\ \mathrm{sgn}(P_{cmd})$$

$$\Delta\phi = \left(\phi - \phi_{cmd}\right)\mathrm{sgn}(P_{cmd}) \quad \ldots 0 \le \Delta\phi \le \left|\frac{P_{cmd}}{f_S}\right|$$

Directional CSAS feedback linearisation:

$$F_R = \frac{b_W}{2\,V_T}\left(C_{n\hat{R}}(\alpha) + \frac{I_{xz}}{I_{xx}}C_{l\hat{R}}(\alpha) - C_{n\hat{R}ref}\right)$$

$$F_{\delta_R} = \frac{1}{C_{n\delta_R}(\alpha) + \frac{I_{xz}}{I_{xx}}C_{l\delta_R}(\alpha)}$$

$$F_{qz} = \frac{I_{zz}}{q_\infty S_W\, b_W}$$

Directional CSAS command shaping:

$$R_{cmd} = \frac{g}{V_T}\ \sin(\phi_{cmd})$$

$$\beta_{cmd} = \frac{\beta_{max}}{2}\left(\frac{V_I}{V_{ref}}\right)^2\delta_{yaw} \quad \ldots -\beta_{max} \le \beta_{cmd} \le \beta_{max}$$

Lateral-directional feedforward control:

$$F_{P\beta} = C_{l\beta}(\alpha) + \frac{I_{xz}}{I_{zz}}C_{n\beta}(\alpha)$$

$$F_{RP} = \frac{b_W}{2V_T}\cdot\frac{I_{xz}}{I_{xx}}C_{l\hat{P}}(\alpha)$$

$$F_{AR} = \frac{1}{1 - F_{\delta AR}\,F_{\delta RA}}\begin{bmatrix} 1 & -F_{\delta AR} \\ -F_{\delta RA} & 1 \end{bmatrix}$$

$$F_{\delta AR} = \frac{C_{l\delta_R}(\alpha) + \frac{I_{xz}}{I_{zz}}C_{n\delta_R}(\alpha)}{C_{n\delta_R}(\alpha) + \frac{I_{xz}}{I_{xx}}C_{l\delta_R}(\alpha)}$$

$$F_{\delta RA} = \frac{I_{xz}}{I_{xx}}$$

Acknowledgements

The authors are grateful to the NASA Langley Research Center, specifically Kevin Cunningham and Gautam Shah, for providing the GTT model data.

References

[1] Gary J. Balas. Flight control law design: An industry perspective. *European Journal of Control*, 9(2-3):207-226, 2003. DOI: 10.3166/ejc.9.207-226

[2] Stephen J. Gill, Mark H. Lowenberg, Simon A. Neild, Luis G. Crespo, Bernd Krauskopf, and Guilhem Puyou. Nonlinear dynamics of aircraft controller characteristics outside the standard flight envelope. *Journal of Guidance, Control, and Dynamics*, 38(12):2301-2308, 2015. DOI: 10.2514/1.G000966

[3] Luis G. Crespo, Sean P. Kenny, David E. Cox and Daniel G. Murri. Analysis of control strategies for aircraft flight upset recovery. In *AIAA Guidance, Navigation, and Control Conference*, Minneapolis, MN, Aug. 2012. DOI: 10.2514/6.2012-5026

[4] John V. Foster, Kevin Cunningham, Charles M. Fremaux, Gautam H. Shah, Eric C. Stewart, Robert A. Rivers, James E. Wilborn, and William Gato. Dynamics modeling and simulation of large transport airplanes in upset conditions. In *AIAA Guidance, Navigation, and Control Conference and Exhibit*, San Francisco, CA, Aug. 2005. DOI: 10.2514/6.2005-5933

[5] Kevin Cunningham, Gautam H. Shah, Neal T. Frink, Susan N. McMillin, Patrick C. Murphy, Frank R. Brown, Patrick J. Hayes, Kamal M. Shweyk, and Sudheer N. Nayani. Preliminary test results for stability and control characteristics of a Generic T-tail Transport airplane at high angle of attack. In *AIAA Atmospheric Flight Mechanics Conference*, Kissimmee, FL, Jan. 2018. DOI: 10.2514/6.2018-0529

[6] S. Naomi McMillin, Neal T. Frink, Patrick C. Murphy, Kevin Cunningham, and Gautam H. Shah, and Sudheer N. Nayani. Computational study of a Generic T-tail Transport. In *AIAA Scitech 2019 Forum*, San Diego, CA, Jan. 2019. DOI: 10.2514/6.2019-0036

[7] Daniel Pusztai, Mark H. Lowenberg, and Simon A. Neild. Static wind tunnel testing of a Generic T-Tail Transport airplane at high angle of attack. In *AIAA Scitech 2023 Forum*, National Harbor, MD, Jan. 2023. DOI: 10.2514/6.2023-0217

[8] Daniel Pusztai, Mark H. Lowenberg, and Simon A. Neild. Flight testing of a dynamically scaled transport aircraft model for high-alpha wind tunnel data validation. In *AIAA Scitech 2024 Forum*, Orlando, FL, Jan. 2024. DOI: 10.2514/6.2024-1497

[9] Richard E. Day. Coupling Dynamics in Aircraft: A Historical Perspective. NASA Special Publication SP-532, NASA, Dryden Flight Research Center, Edwards, CA, 1997.